A Geometric Analysis of Diffusion Tensor Measurements of the Human Brain

Andrew L. Alexander,[1]* Khader Hasan,[2] Gordon Kindlmann,[3] Dennis L. Parker,[1] and Jay S. Tsuruda[1]

The degree of diffusion tensor anisotropy is often associated with the organization of structural tissues such as white matter. Numerous measures of diffusion anisotropy have been proposed, which could lead to confusion in interpreting and comparing results from different studies. In this study, a new method for representing the diffusion tensor shape, called the three-phase (3P) plot, is described. This is a graphical technique based upon a barycentric coordinate system, which weights the tensor shape by a combination of linear, cylindrical, and spherical shape factors. This coordinate system can be used to map and potentially segment different tissues based upon the tensor shape. In addition, the 3P plot can be used to examine the shape properties of existing measures of diffusion anisotropy. In this paper, the 3P plot is used to compare four well-known anisotropy measures: the anisotropy index, the fractional anisotropy, the relative anisotropy, and the volume fraction. Computer simulations and diffusion tensor images of normal brains were obtained to study the properties of this new mapping technique. **Magn Reson Med 44:283–291, 2000.** © 2000 Wiley-Liss, Inc.

Key words: diffusion tensor; anisotropy; white matter; human brain

Diffusion-tensor MRI (DT-MRI) is a noninvasive imaging technique for visualizing the structural characteristics of deep tissues (1). DT-MRI has been used to elucidate the structural geometry of organized tissues such as structural muscle tissue (2,3), bone marrow (4), the heart (5,6), the brain (7–10), intervertebral discs (11), and the spinal cord (12–14). The diffusion tensor not only describes the magnitude of the water diffusion, but also the degree and the principle directions of anisotropic diffusion. Attempts to quantify and visualize properties of the diffusion tensor have resulted in scalar measures of average diffusivity and diffusion anisotropy. These measures may be useful for discriminating between normal and pathologic tissue types or states.

A common measure of the diffusion magnitude is the trace of the diffusion tensor. The trace is an invariant measure of diffusivity and is independent of the encoding axes used in the diffusion measurements. The trace of the diffusion tensor has shown great promise in evaluating brain ischemia and stroke (15–18).

The anisotropy of the diffusion tensor is the degree to which the tensor deviates from the spherically isotropic case. Conceptually, measures of diffusion anisotropy attempt to reduce the shape description of the 3D diffusion tensor to a single scalar value. The diffusion anisotropy is related to the structural organization of the tissue (1). The degree of diffusion anisotropy can be used to discriminate between white matter (highly anisotropic diffusion) and gray matter (less anisotropic diffusion) in the brain. Recent studies have shown that measurements of the diffusion anisotropy can be used to study white matter morphology (19), white matter trauma (20), and the development of white matter tracts in infants (21,22).

Numerous measures of diffusion anisotropy have been proposed (1,9,23–26). These include various combinations of orthogonal diffusion measurements and rotationally invariant measures based upon the eigenvalues of the diffusion tensor. Pierpaoli et al. demonstrated that only rotationally invariant measures of the diffusion anisotropy can accurately quantify the tensor anisotropy when the principle axes of the tensor are not aligned with the measurement axes (23). The relationship between tensor shape and many of these invariant measures of the anisotropy are not well-defined. For a specific application in which the goal is to detect tissue structures with different diffusion tensor shapes (e.g., gray matter vs. white matter, or diseased white matter vs. normal white matter), the optimum measure of diffusion anisotropy will be the one that is most sensitive to the shape differences.

In this paper, we will examine the geometric dependencies of normalized anisotropic measures that are rotationally invariant. By normalized, we mean that the anisotropy measures range between 0 and 1 for the isotropic and completely anisotropic cases, respectively. A barycentric (3-phase) plot will be used to relate each of the anisotropy measures to the tensor shape. First, the theoretical, noise-free case will be described. The effects of noise on the measures of diffusion anisotropy will then be evaluated using both simulations and experimental measurements. Finally, we will describe the criteria for selecting the optimum anisotropy measure for specific applications.

Geometric Description of the Diffusion Tensor Anisotropy

The geometric shape associated with a diffusion tensor, $\underline{\mathbf{D}}$, is assumed to be a 3D ellipsoid with lengths of the three orthogonal principle axes proportional to the sorted tensor eigenvalues (in decreasing order) – λ_1, λ_2, and λ_3. The ellipsoidal shape arises from the isosurface of the multivariate normal probability distribution of diffusivity (27),

$$p(x|x_o, \tau) = \frac{1}{\sqrt{(4\pi\tau)^3|\underline{\mathbf{D}}|}} \exp\left[\frac{-(x - x_o)^T\underline{\mathbf{D}}^{-1}(x - x_o)}{4\tau}\right] \quad [1]$$
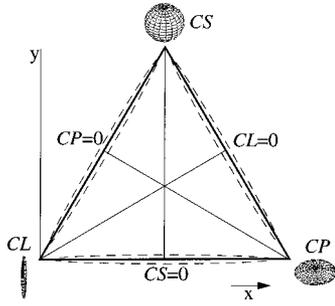
FIG. 1. Three-phase (3P) tensor shape diagram. Any 3D ellipsoid can be defined by triangulating the normal distances of any two shape parameters. $x = (1 - CL + CP)/1.732$; $y = 1 - CL - CP$

where the diffusion tensor, behaves like a covariance matrix describing the displacement, τ is the diffusion time, and x is the position relative to the center of the distribution, x_o. The sum of the eigenvalues is equal to the trace of the diffusion tensor

$$tr\{\underline{\mathbf{D}}\} = 3\langle\lambda\rangle = \lambda_1 + \lambda_2 + \lambda_3 \qquad [2]$$

where $\langle\lambda\rangle$ is the mean eigenvalue.

A convenient way to represent the shape of the diffusion tensor is as a combination of basis shapes as described by Westin et al. (25). In their work, they demonstrated that the diffusion tensor can be described by a combination of linear, planar, and spherical measures:

$$CL = \frac{\lambda_1 - \lambda_2}{3\langle\lambda\rangle}, \qquad [3]$$

$$CP = \frac{2(\lambda_2 - \lambda_3)}{3\langle\lambda\rangle}, \qquad [4]$$

and

$$CS = \frac{\lambda_3}{\langle\lambda\rangle}. \qquad [5]$$

The normalization by the ADC causes each measure to range between 0 and 1. In addition, the sum of the three shape measures is 1. Since their sum is a constant value, the shape can be described completely by any two of the three shape measures. One method to represent the shape would be to plot any two of the measures on orthogonal axes, such as CP versus CL. This approach, however, will emphasize the differences between linear and planar anisotropy more strongly than between spherical and either linear or planar anisotropy.

An alternative method for representing shape is to plot all three variables on a three-phase (3P) plot, which uses a barycentric coordinate system (28,29), as shown in Fig. 1. The advantage of this representation is that the effective distances between each of the three shape cases are equivalent. Each shape measure is plotted as the distance perpendicular from a side. The position for a 3D ellipsoid shape on the 3P plot is found by triangulating any of the two shape measures. The left and right sides of the 3P triangle correspond to cylindrically symmetric diffusion tensors.

The 3P plot may be used to visualize the shape dependence of tensor anisotropy measures. Several anisotropy measures have been described in the literature. Westin et al. (25) describe an anisotropy index, CA, as the sum of the linear and planar shape measures,

$$CA = CL + CP = 1 - CS. \qquad [6]$$

Basser and Pierpaoli also have described several measures of diffusion anisotropy (1,23). In this paper, we will examine three of the anisotropy measures. The relative anisotropy,

$$RA = \frac{\sqrt{(\lambda_1 - \langle\lambda\rangle)^2 + (\lambda_2 - \langle\lambda\rangle)^2 + (\lambda_3 - \langle\lambda\rangle)^2}}{\sqrt{6}\,\langle\lambda\rangle} \qquad [7]$$

is the RMS difference between the eigenvalues and the eigenvalue mean normalized by the eigenvalue mean (equivalent to A_σ, defined by Conturo et al. (24)). The fractional anisotropy,

$$FA = \sqrt{\frac{3((\lambda_1 - \langle\lambda\rangle)^2 + (\lambda_2 - \langle\lambda\rangle)^2 + (\lambda_3 - \langle\lambda\rangle)^2)}{2(\lambda_1^2 + \lambda_2^2 + \lambda_3^2)}} \qquad [8]$$

is a similar RMS difference measure normalized by the RMS of the eigenvalues. The third measure, the volume ratio,

$$VR = \frac{\lambda_1\lambda_2\lambda_3}{\langle\lambda\rangle^3} \qquad [9]$$

is the ratio of the tensor ellipsoid volume to the volume of a sphere with the same eigenvalue mean. To compare this measure with the others, we define a measure called the volume fraction,

$$VF = \frac{\langle\lambda\rangle^3 - (\lambda_1\lambda_2\lambda_3)}{\langle\lambda\rangle^3} = 1 - VR. \qquad [10]$$

The values of CA, RA, FA, and VF are each normalized to range between 0 and 1, with 0 corresponding to isotropic diffusion and 1 being the most anisotropic case for that measure.

It is clear that the behaviors of CA, RA, FA, and VF are slightly different, yet they all depend upon the same set of measured parameters – λ_1, λ_2, and λ_3. To examine the dependence of an anisotropy measure on the tensor geometry, the amplitude of an anisotropy measure can be plotted as an intensity on the 3P plot. This is illustrated in Fig. 2 where the brightest voxels correspond to the anisotropy = 1 case, the darkest voxels corresponds to the isotropic case and the gray intensities correspond to intermediate anisotropy values. It is clear from these intensity maps that each anisotropy measure has significantly different dependencies on the tensor shape. In particular, each anisotropy measure is weighted very differently by the planar anisotropy.
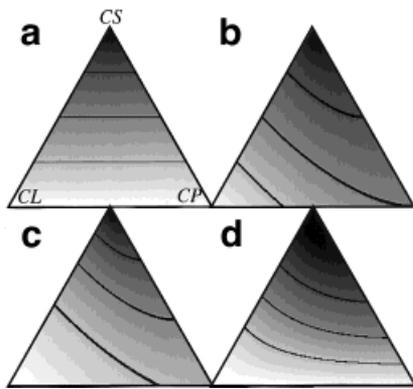
FIG. 2. Parametric intensity maps of the *CA* (**a**), *RA* (**b**), *FA* (**c**), and *VF* (**d**) anisotropy measures. The 0.25, 0.5, and 0.75 anisotropy levels are indicated as isocontours for each measure.

This geometric approach may also be of significant value in determining the best measure to use for detecting the differences between the diffusion tensors of two or more tissues. For the task of discriminating between two tissue classes, a measure of diffusion anisotropy, *A*, can be evaluated using a detectability index,

$$d = \frac{<A_1> - <A_2>}{\sqrt{\sigma_1^2 + \sigma_2^2}}, \qquad [11]$$

where $<A_1>$, $<A_2>$, σ_1^2, and σ_2^2 are the means and variances of the anisotropy values for the two tissue classes. The anisotropy measure with the greatest detectability index should be close to optimum for the specified task. The variances depend upon a combination of tissue and subject variability, measurement noise, the encoding axes, the diffusion weighting and the pulse sequence parameters (TR, TE, etc.). It is well known that these measures of diffusion anisotropy are highly sensitive to measurement noise and as such any study of diffusion anisotropy must take noise effects into account.

METHODS

Noise Simulations

Computer simulations were performed using Matlab (The Mathworks, Inc., Natick, MA) to study the effects of measurement noise on the measures of diffusion anisotropy. These simulations are similar to the Monte Carlo techniques used by Pierpaoli and Basser (23) and Bastin et al. (30). For a given diffusion tensor, a simulated diffusion tensor imaging experiment was performed in which the noise-free signals for the specified gradient encoding were first calculated. Gaussian random noise with zero mean and a specified variance (e.g., amount of noise) was independently added to each of the encoded signals and the absolute value was determined. The sorted eigenvalues of **D**, and the anisotropy measures (*CA*, *RA*, *FA*, and *VF*) were estimated from the noisy tensor signal measurements. The process was repeated 6000 times with new random noise values added for each repetition. The mean and standard deviation of the eigenvalues and anisotropy measures

were determined. The signal-to-noise ratio was calculated as the signal intensity of the signal without diffusion weighting divided by the square-root of the noise variance.

For this study, the dual-gradient diffusion encoding described by Basser and Pierpaoli (31) was simulated to best match the protocol used in the imaging studies. The diffusion weighting, b, was set to 900 sec/mm². The ADC of the simulated diffusion tensors was assumed to be 2.1 x 10^{-3} mm²/sec, which is similar to the values for normal gray matter and white matter. The effects of noise on the anisotropy measures was investigated over a range of signal-to-noise ratios between 5 and 100. Although we did not perform an exhaustive simulation of the entire geometric space, representative cases were examined to determine the effects of measurement noise. Specifically, we examined the cases of varying degrees of cylindrical ($\lambda_1 > \lambda_2 \sim \lambda_3$) and laminar ($\lambda_1 \sim \lambda_2 > \lambda_3$) diffusion.

Imaging Experiments

Diffusion-tensor imaging (DTI) was performed on five volunteers. Informed consent was obtained from all subjects in accordance with the guidelines of our institutional review board for human subject studies. Images were obtained using a SIGNA 1.5 T scanner (General Electric Medical Systems, Milwaukee, WI) equipped with Echospeed imaging gradients (22 mT/m maximum amplitude with 120 mT/m/msec slew rate). The product spin-echo EPI pulse sequence was modified to obtain a set of images with the prescribed diffusion-encoding gradients. The imaging parameters used were TR = 6000 msec, TE = 90 msec, and field-of-view = 240 × 240 mm². The echo planar readout was performed with ramp sampling, 80/128 fractional ky encoding (0.5 NEX with 16 overscans) and a homodyne Fourier reconstruction to form a 128 × 128 voxel image matrix. Ten adjacent coronal slices (4-mm thick) were prescribed. The resultant voxel dimensions were 1.875 × 1.875 × 4.0 mm³. The amplitude, width, and spacing of the diffusion gradient pulses were $\sqrt{2} \times 22 = 31.1$ mT/m, 25 msec, and 31 msec, respectively, yielding an effective diffusion-weighting of b = 1002 sec/mm². The pulse sequence was configured to obtain seven sets of diffusion encoded images with (Gx, Gy, Gz) = (0,0,0), (0.707, 0, 0.707), (−0.707, 0, 0.707), (0,0.707,0.707), (0,0.707,−0.707), (0.707, 0.707, 0), and (−0.707, 0.707, 0) where Gx, Gy, and Gz were the relative scales of the total diffusion gradient amplitude (31.1 mT/m) in the x, y, and z directions, respectively. The acquisition for each encoding direction was repeated seven times for later averaging to improve the SNR. This corresponded to 49 images per slice or 490 images total in a single series. The total acquisition time was 6 minutes, 16 seconds. The raw diffusion weighted images were reconstructed on the scanner then copied to a remote SUN workstation for image processing.

Diffusion Tensor Image Analysis

First, the seven repeated images in each diffusion encoding direction were averaged to a single image to improve the image signal-to-noise ratio. The images were then registered to correct for eddy current distortions. Eddy currents caused by the large diffusion-encoding gradients can

cause significant distortion in echo planar images. This distortion is dependent upon the diffusion-encoding direction and may cause significant errors in the calculations associated with the diffusion tensor, particularly for voxels near the periphery of the brain. Previously, we described bipolar gradient pulse techniques to minimize these distortions (32). However, these techniques are less efficient than unipolar diffusion-gradient techniques, therefore we decided to use unipolar diffusion gradients for this study. The resultant image distortions were corrected using a retrospective correction algorithm similar to that of Haselgrove et al. (33). This technique appears to greatly improve registration between the different diffusion-encoded images.

After the diffusion-encoded images were registered, the diffusion coefficient, D_i, in each encoding direction, i, was then calculated by

$$D_i = \frac{\ln(S_o) - \ln(S_i)}{b}, \qquad [12]$$

where S_o and S_i are the intensities of the reference ($b \cong 0$) and diffusion-encoded images, respectively. The diffusion tensor elements were calculated from the encoded diffusion coefficients as described by Basser et al. (31). Because the tensor was assumed to be symmetric about the diagonal, the full 3×3 tensor could be estimated from six diffusion-encoded measurements. Eigenvalue decomposition of each voxel tensor was performed to determine the principle ordered eigenvalues, λ_1, λ_2, and λ_3. The tensor shape parameters, *CL*, *CP*, and *CS*, and the anisotropy measures, *CA*, *RA*, *FA*, and *VF*, were calculated at each voxel location from the eigenvalues using Equations 3–10. The diffusion tensor image processing was performed using software developed using IDL (Research Systems, Boulder, CO) on a SUN workstation.

To compare anisotropy measures, measurements of *CL*, *CP*, *CA*, *RA*, *FA*, and *VF* at user-specified voxels were obtained. The *FA* parametric image was used to select voxels in specific gray matter, deep nuclei and white matter regions - cortical gray matter, thalamus, lentiform nucleus (putamen and globus palladus), corpus callosum, internal capsule, arcuate fasciculus, and subcortical (corona radiata and U association) white matter fibers. Approximately the same number of samples were selected from each subject. For each tissue class, the means and standard deviations for the anisotropy and shape measures were estimated from the pooled multi-subject data.

RESULTS

From our coronal DTI protocol, we estimated that the SNR of gray and white matter regions in the non-DW images (b = 0) was between 20 and 26. This was accomplished by calculating the mean and standard deviation of the six reference images and taking the ratio. The estimated SNR for the averaged reference images increased by a factor of $\sqrt{7} = \sqrt{NEX}$ to lie in the range between 53 and 69. Consequently, we focused on the noise simulations for an SNR of 60, which near the center of this range. The results of the noise simulations for varying degrees of linear an-
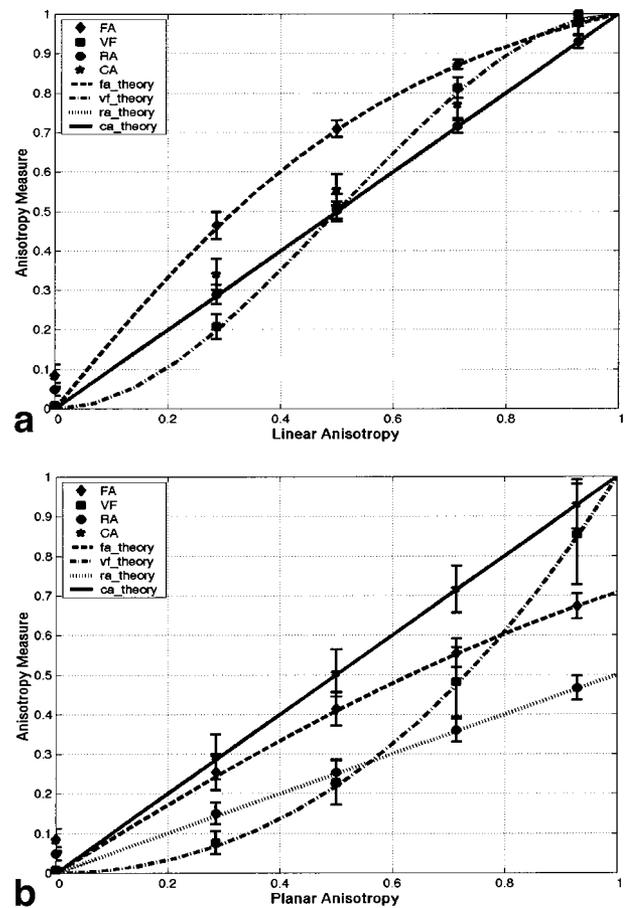

FIG. 3. Plots of simulated (symbols) and theoretical (lines) anisotropy measures as a function of varying degrees of (**a**) spherical to linear anisotropy and (**b**) spherical to planar anisotropy. These plots correspond to the left and right sides of the 3P triangle in Fig. 1 and correspond to the cases of axially symmetric diffusion tensors. Note that the theoretical plots of *RA* and *CA* for linear anisotropy are identical.

isotropy corresponding to the left edge of the 3P diagram are shown in Fig. 3a. It is interesting to note that the *CA* anisotropy index demonstrates the greatest bias (deviation from predicted values) in these measurements. This is because noise causes estimates of λ_1 to be overestimated and λ_3 to be underestimated (23,30), resulting in a general overestimation bias in the estimate of the planar anisotropy term, which should be zero in the absence of noise. For the completely isotropic case, all of the anisotropy measures, except the *VF*, demonstrate significant bias for the same reason. The biases and standard deviations both increase as the SNR is decreased; however, the trends observed in Fig. 3 remain unchanged. The noise simulations for varying degrees of planar anisotropy (the right edge of the 3P diagram) are shown in Fig. 3b. Except for the completely isotropic case, there does not appear to be a significant bias caused by any of the anisotropy measures. However, the standard deviation of the *VF* measure appears much larger than for the other measures. Aside from biases and standard deviations, these curves also illustrate the large variation in the theoretical behavior of these
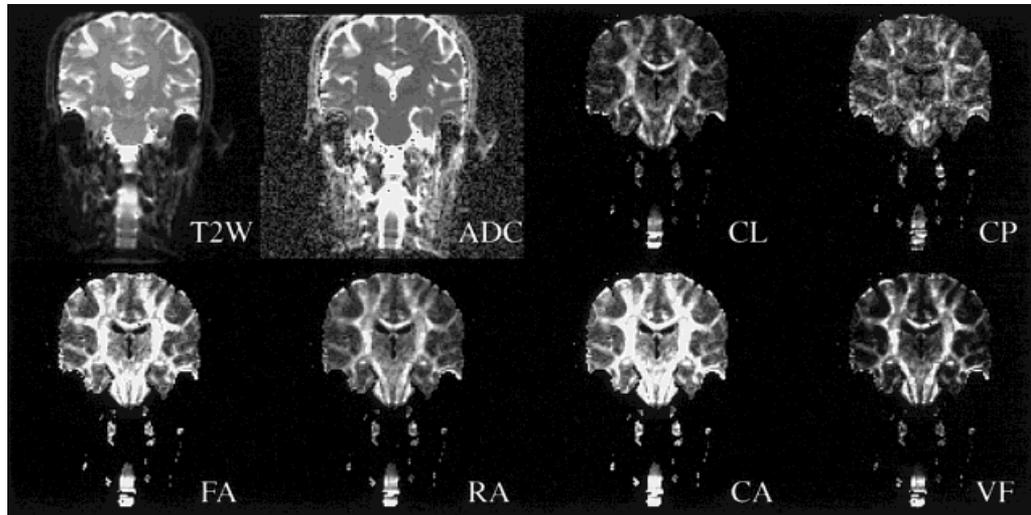
FIG. 4. Parametric diffusion tensor maps for one image slice. The images include the T_2-weighted (T2W) reference image and the tensor trace map. The parametric maps of the shape and anisotropy measures show significantly different gray matter versus white matter detail. The commissural (corpus callosum) and projection (internal capsule) white matter fibers are emphasized on the *CL* map. The association white matter fibers appear to have a significant planar tensor component. All parametric maps (0 to 1) are scaled to the same relative gray scale range (0 to 255).

anisotropy measures, reinforcing the anisotropy level dependencies shown in Fig. 2. These curves however, only describe the behavior of the measures along the sides of the 3P space. It is likely that most measurements will be located somewhere between behavior displayed in the two plots in Fig. 3.

The parametric tensor images of a slice from the DT study of one subject is shown in Fig. 4. The parametric anisotropy images (Fig. 4, bottom row) illustrate that the white matter features appear different for each of the anisotropy measures. These differences arise from the relative contributions from the linear and planar shape components of the diffusion tensor. In all of the images, regions of cortical gray matter appear dark. Conversely, the commissural (corpus callosum) and projection (corticospinal and internal capsule) white matter tracts appear brightest in all of the anisotropy images. The association (arcuate fasciculus & subcortical) white matter tracts demonstrate much more variability on the parametric anisotropy images. Maps of the linear and planar tensor shape components (Fig. 4, top row) illustrate that the commissural and projection white matter tracts are highly linear, whereas, many of the association white matter fibers, the arcuate fasciculus in particular, have significant planar shape contributions.

Figure 5 shows the measurements of the geometric tensor shape parameters of gray matter, deep nuclei and white matter regions (labeled in Fig. 6) for the four sets of volunteer images as plotted in 3P space. The plot is highly cluttered, but illustrates that the clustering and range of tensor shapes observed in the human brain. The mean location and covariance matrix was estimated from all the samples in each class. The bivariate normal distributions associated with the estimated covariance matrices are represented on the 3P plot in Fig. 7 by one standard deviation isocontours. Note that the isocontours do not illustrate the

full extent of all the samples. For example, some corpus callosum samples have a much higher *CL* than is described by the contour region. Similarly, several arcuate fasciculus and subcortical white matter samples appear to have a greater *CP* component. Gray matter measurements appear clustered near the top of the plot indicating the isotropic diffusion properties of these tissues. Deep nuclei (thalamus and lentiform) regions also contain some axon connections and are slightly more anisotropic. The next most anisotropic tissue groups are the association white matter fibers—arcuate fasciculus and subcortical U fibers. The corpus callosum and internal capsule are the most highly anisotropic tissues with highly linear anisotropy.
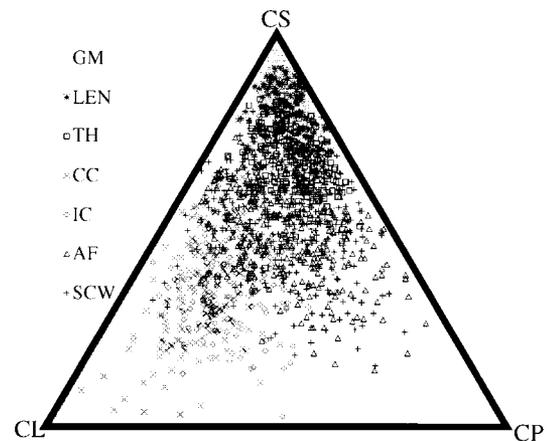

FIG. 5. Estimated *CL* and *CP* values for the tensor measurements of specific tissues in four individuals are plotted in 3P coordinates. There is an obvious overlap of measured tensor shapes for the tissue classes. The plot also shows that there are measurements in much of the 3P space including measurements with high planar anisotropy.
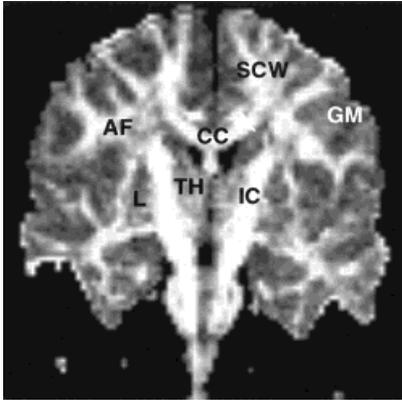
FIG. 6. A single slice *FA* map with the corresponding regions that were sampled. All regions are bilateral and were sampled accordingly. CC = corpus callosum, IC = internal capsule, AF = arcuate fasciculus, SCW = subcortical white matter, TH = thalamus, L = lentiform. The cortical gray matter (GM) in general was assumed to be the dark gray regions near the surface of the head.

The distributions of tensor shape for each of the tissue classes were compared using a general linear model (SAS 6.12 statistical analysis software package; SAS Institute, Cary, NC). The *CL* distributions for all tissue classes was found to be significantly different from all other classes ($P < 0.0001$). The *CP* shape measure was able to distinguish between all classes except the comparison between subcortical and arcuate fasciculus. The distributions for each of the anisotropy measures were also compared; and all classes were separable for each measure. The generalized linear model had the best fit for the *FA* measure ($R^2 = 0.824$).

The mean and standard deviation of *CL* and *CP* as a function of the tissue is listed in Table 1. Also listed are *CL* and *CP* values that were estimated from the reported mean eigenvalues of tissues in studies by Pierpaoli et al. (10) and Shimony et al. (34). These estimates show that corpus callosum has the greatest linear component to the tensor shape, whereas arcuate fasciculus has the greatest planar component. Table 2 lists the mean and standard deviation of the anisotropy measures for each of the tissue classes. All of the anisotropy measures show the same tissue class hierarchy of increasing anisotropy. Table 3 compares the estimated detectability indices (Eq. [11]) for each of the estimated values of tensor shape (Table 1) and anisotropy (Table 2) for several tissue comparisons. The ability to distinguish the tissue groupings by a specific anisotropy measure should increase with the magnitude of the detectability index. The fractional anisotropy measure showed the greatest separability in the majority of cases. As the tissue distributions in Fig. 7 illustrate, the maximum separability in the 3P coordinate system may oblique to either of the *CL*, *CP,* or *CA* (= 1 – *CS*) axes. The maximum separability in 3P space was estimated by using a bivariate distance measurement

$$d_{3P} = \sqrt{(x_1 - x_2)^T (\Sigma_1 + \Sigma_2)^{-1} (x_1 - x_2)} \qquad [13]$$

where x_1 and x_2 are the mean 3P coordinates of tissue classes 1 and 2. Σ_1 and Σ_2 are the corresponding covari-

ance matrices. These distances are also listed in Table 3. This distance is greater than or equal to the *CL*, *CP*, and *CA* measures in all cases. However, the separability for the *FA* measure is still greater than the 3P distances in many of the cases.

DISCUSSION

Diffusion tensor measurements of brain tissues contain a wealth of information. The shape of a tensor can be represented by the relative eigenvalues of the tensor. Numerous measures of tensor anisotropy, which attempt to describe attributes of the tensor shape in a single scalar value, have been proposed. Each of these measures is a function of these three eigenvalues. While it is clear that these different anisotropy measures emphasize different tensor features, the relationship between these measures has not been fully described. By mapping the intensities of diffusion anisotropy measures in the 3P coordinate system (see Fig. 2), the tensor shape properties of anisotropy measures can be visualized. These maps may be used to explain the differences in contrast between the anatomic features shown in brain anisotropy images as shown in Fig. 4.

By mapping measurements of the tensor shape of known tissues in the 3P space, the distributions of tensor shape properties can be estimated and used to compare the tensor shape properties between different brain tissues. In our study, we demonstrated that there was a tensor shape hierarchy for tissue groups in the order of gray matter, deep nuclei, association white matter, deep projection white matter and commissural white matter. Despite their differences, all of the diffusion tensor anisotropy measures showed the same tissue order of increasing anisotropy. However, some measures were better than others in discriminating between different tissue types. In general, *FA*

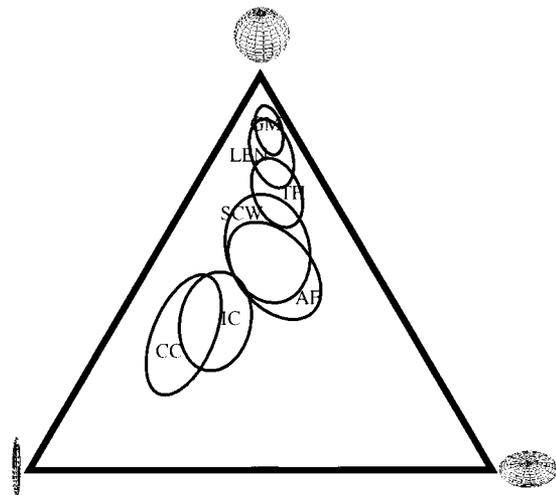FIG. 7. Bivariate normal distributions of the tissue shape measurements were estimated from the sample points in Fig. 5. Isocontours of one standard deviation from the mean location in 3P space are plotted. The distributions are highly overlapping in three groups of tissues: 1) corpus callosum and internal capsule, 2) arcuate fasciculus and subcortical white matter, and 3) gray matter, lentiform nucleus and thalamus.

Table 1
Estimated Mean and Standard Deviation of the *CL* and *CP* Shape Measures for Each of the Tissue Groups

	CL	*CL*[A]	*CL*[B]	*CP*	*CP*[A]	*CP*[B]
GM (N = 737)	**0.047**	**0.032**	**0.077**	**0.086**	**0.057**	**0.121**
Standard deviation	0.030			0.049		
LEN (N = 128)	**0.074**	**0.050**		**0.124**	**0.091**	
Standard deviation	0.053			0.073		
TH (N = 172)	**0.112**	**0.063**		**0.190**	**0.109**	
Standard deviation	0.056			0.083		
SCW (N = 474)	**0.204**	**0.176**	**0.332**	**0.233**	**0.234**	**0.347**
Standard deviation	0.106			0.116		
AF (N = 281)	**0.217**			**0.275**		
Standard deviation	0.094			0.136		
IC (N = 168)	**0.403**	**0.352**	**0.455**	**0.213**	**0.287**	**0.325**
Standard deviation	0.103			0.091		
CC (N = 145)	**0.493**	**0.433**	**0.668**	**0.158**	**0.221**	**0.173**
Standard deviation	0.128			0.076		

The first *CL* and *CP* columns correspond to the measurements from this study. These values may be compared with the estimated average *CL* and *CP* based upon measured eigenvalues of brain tissues from other studies: A, Shimony et al. (34); B, Pierpaoli et al. (10); GM, gray matter; LEN, lentiform nucleus; TH, thalamus; SCW, subcortical white matter; AF, arcuate fasciculus; IC, internal capsule; CC, corpus callosum. N is the total number of sampled points for all four subjects.

was the best anisotropy measure for separating most of the defined classes. In fact, the *FA* was generally better than the optimum distance measure in 3P space. This is because *FA* has a nonlinear mapping into the 3P coordinates. The tissue distributions near the top of the plot (more spherical–corresponding to gray matter and regions of nuclei) were narrower and spaced closer together. The *FA* mapping in this region spreads out these distributions relative to the more anisotropic tissues. The *FA* anisotropy measure clearly shows good contrast between gray and white matter regions. The deep nuclei are slightly brighter than gray matter. The thalamus and lentiform regions contain both nuclei and axons, thereby increasing the anisotropy somewhat over that of gray matter.

One potential limitation with our analysis is that the *FA* map was used to select voxel locations for each of the tissue classes, which may slightly bias the detectability index results preferentially towards the *FA* measure. Care was taken to select a range of voxel anisotropy values to avoid just selecting the brightest and darkest voxels in a

Table 2
Comparison of Estimated Means and Standard Deviations of the Anisotropy Measures as a Function of Tissue Type

	CA	*FA*	*RA*	*VF*
GM (N = 737)	**0.135**	**0.140**	**0.081**	**0.022**
Standard deviation	0.058	0.057	0.034	0.021
LEN (N = 128)	**0.201**	**0.209**	**0.123**	**0.051**
Standard deviation	0.083	0.086	0.054	0.048
TH (N = 172)	**0.304**	**0.308**	**0.184**	**0.107**
Standard deviation	0.083	0.079	0.051	0.057
SCW (N = 474)	**0.439**	**0.453**	**0.287**	**0.243**
Standard deviation	0.131	0.127	0.096	0.139
AF (N = 281)	**0.494**	**0.496**	**0.317**	**0.291**
Standard deviation	0.123	0.099	0.077	0.127
IC (N = 168)	**0.619**	**0.667**	**0.469**	**0.499**
Standard deviation	0.118	0.102	0.097	0.154
CC (N = 145)	**0.653**	**0.728**	**0.539**	**0.583**
Standard deviation	0.146	0.112	0.128	0.187

Abbreviations as in Table 1.

region. In general, the contrast between white matter tracts and gray matter is most visually apparent for the *FA* measure. If a different anisotropy measure had been used to select the voxels, we predict that the detectability indices may shift slightly in favor of the anisotropy measure used for the selection. Even with slight shifts in the indices, we predict that the *FA* measure will still demonstrate the greatest class separability.

In this study, we chose to examine four common measures of diffusion tensor anisotropy. The characterization could easily be extended to any anisotropy measure including those recently described by Ulug and van Zijl (26). In addition, the use of the 3P plot does not preclude the use of non-analytic measures. In fact, any arbitrary mapping of the 3P space can be used to create image maps that highlight any set of specific tensor shape features.

The linear and planar shape measures emphasize different white matter features. The commissural and deep projection (internal capsule and corticospinal) white matter tracts are the features with the greatest linear shape dominance. Both the arcuate fasciculus and peripheral radiation fibers also appear to have a significant planar component to their tensor measurements. The causes of planar diffusion in the brain are not perfectly understood. Tissue membranes arranged in sheets could explain planar diffusion; however, a more likely origin is the crossing and twisting of white matter fibers and overlap of gray matter tissues within a signal voxel. In addition, estimates of the planar contribution may be slightly inflated by the underestimation of λ_3 in noisy data. However, the effects of noise on the eigenvalues cannot completely account for the large spread of shape measures in the 3P space. It is likely that the planar features will decrease for images with smaller voxel sizes and higher SNR.

Conturo et al. (24) demonstrated that the diffusion tensor could be estimated from four encoding measurements (tetrahedral encoding) if the diffusion was axially or cylindrically symmetric. The left and right sides of the 3P plot correspond to the cylindrically symmetric cases.

Table 3
Estimated Detectabilities, d, Between Selected Tissue Groups for Each of the Shape and Anisotropy Measures

	GM vs. CC	GM vs. AF	GM vs. SCW	TH vs. IC	LEN vs. IC	AF vs. CC	CC vs. IC	AF vs. SCW
CL	3.39	1.72	1.43	2.48	2.84	**1.74**	**0.55**	0.09
CP	0.80	1.31	1.17	0.19	0.76	0.75	0.46	0.23
CA	3.30	2.64	2.12	2.18	2.90	0.83	0.18	**0.31**
FA	**4.68**	**3.12**	**2.25**	**2.78**	**3.43**	1.55	0.40	0.27
RA	3.46	2.80	2.02	2.60	3.12	1.49	0.44	0.24
VF	2.98	2.09	1.57	2.39	2.78	1.29	0.35	0.25
d_{3P}	3.49	2.83	2.15	2.62	3.16	**1.76**	**0.66**	**0.31**

The anisotropy measure with the greatest separability is highlighted in boldface. Abbreviations as in Table 1.

However, diffusion tensor measurements in the human brain span much of the 3P space and, therefore, do not demonstrate cylindrical symmetry. Consequently, a minimum of six diffusion gradient encoding axes are required to estimate the full 3x3 diffusion tensor. Our measurements of *CL* and *CP* for different tissues are in good agreement with the estimated values from the data of Shimony et al. (34). The estimated shape measurements from the data of Pierpaoli et al. (10) tend to be larger, although the trend as a function of the tissue type is consistent with our measurements.

One potential limitation with the study is that we have ignored the effects of intravoxel partial volume contamination, which is likely in EPI studies with large voxel dimensions (35–37). CSF contamination can be reduced by nulling the signal with an inversion recovery technique, such as FLAIR (35,36). Diffusion tensor studies performed with and without CSF signal suppression demonstrated significant differences in the tensor trace values for regions of CSF contamination. However, regions of GM with CSF contamination did not show a significant increase in anisotropy with CSF suppression. A careful partial volume analysis of gray matter and white matter showed that the diffusion tensor trace values for GM and WM are not significantly different; however, an analysis of anisotropy or tensor shape was not performed (37). Further experiments need to be performed to investigate the effects of partial volume contamination on the diffusion tensor shape in brain tissues.

As we have illustrated in this study, Eqs. [3]–[5] are normalized and coupled so that the measurement of any two shape measures can be used to determine the third. This has enabled us to map the 3D ellipsoidal shape in a barycentric coordinate system. We selected the tensor trace divided by three as our normalization factor. There are other sets of normalized shape measures that can be used to map the tensor shape. For example, Westin et al. (25) also described a set of shape measures normalized by the largest eigenvalue. Recently, Bahn (38) described an eigenvalue normalization scheme that was used to reduce the three eigenvalues into two dimensions. Finally, Conturo et al. (24,34) attempted to describe tensor shape by defining the major and minor anisotropy measures. These measures define the variation in ellipsoid shape in terms of the major and minor tensor axes.

REFERENCES

1. Basser PJ, Pierpaoli C. Microstructural and physiological features of tissues elucidated by quantitative-diffusion-tensor MRI. J Magn Reson B 1996;111:209–219.
2. van Doorn A, Bovendeerd PH, Nicolay K, Drost MR, Janssen JD. Determination of muscle fibre orientation using diffusion-weighted MRI. Eur J Morphol 1996;34:5–10.
3. van Donkelaar CC, Kretzers LJ, Bovendeerd PH, Lataster LM, Nicolay K, Janssen JD, Drost MR. Diffusion tensor imaging in biomechanical studies of skeletal muscle function. J Anat 1999;194:79–88.
4. Baur A, Stabler A, Bruning R, Bartl R, Krodel A, Reiser M, Deimling M. Diffusion-weighted MR imaging of bone marrow: differentiation of benign versus pathologic compression fractures. Radiology 1998;207:349–356.
5. Hsu EW, Muzikant AL, Matulevicius SA, Penland RC, Henriquez CS. Magnetic resonance myocardial fiber-orientation mapping with direct histological correlation. Am J Physiol 1998;274:H1627–H1634.
6. Reese TG, Weisskoff RM, Smith RN, Rosen BR, Dinsmore RE, Wedeen VJ. Imaging myocardial fiber architecture in vivo with magnetic resonance. Magn Reson Med 1995;34:786–791.
7. Douek P, Turner R, Pekar J, Patronas N, Le Bihan D. MR color mapping of myelin fiber orientation. J Comput Assist Tomogr 1991;15:923–929.
8. Coremans J, Luypaert R, Verhelle F, Stadnik T, Osteaux M. A method for myelin fiber orientation mapping using diffusion-weighted MR images. Magn Reson Imaging 1994;12:443–454.
9. Peled S, Gudbjartsson H, Westin CF, Kikinis R, Jolesz FA. Magnetic resonance imaging shows orientation and asymmetry of white matter fiber tracts. Brain Res 1998;780:27–33.
10. Pierpaoli C, Jezzard P, Basser PJ, Barnett A, Di Chiro G. Diffusion tensor MR imaging of the human brain. Radiology 1996;201:637–648.
11. Hsu EW, Setton LA. Diffusion tensor microscopy of the intervertebral disc anulus fibrosus. Magn Reson Med 1999;41:992–999.
12. Gulani V, Iwamoto GA, Jiang H, Shimony JS, Webb AG, Lauterbur PC. A multiple echo pulse sequence for diffusion tensor imaging and its application in excised rat spinal cords. Magn Reson Med 1997;38:868–873.
13. Fenyes DA, Narayana PA. In vivo diffusion tensor imaging of rat spinal cord with echo planar imaging. Magn Reson Med 1999;42:300–306.
14. Ford JC, Hackney DB, Alsop DC, Jara H, Joseph PM, Hand CM, Black P. MRI characterization of diffusion coefficients in a rat spinal cord injury model. Magn Reson Med 1994;31:488–494.
15. Moseley ME, Butts K, Yenari MA, Marks M, de Crespigny A. Clinical aspects of DWI. NMR Biomed 1995;8:387–396.
16. Lovblad K, Laubach H, Baird A, Curtin F, Schlaug G, Edelman R, Warach S. Clinical experience with diffusion-weighted MR in patients with acute stroke. Am J Neuroradiol 1988;19:1061–1066.
17. de Crespigny AJ, Marks MP, Enzmann DR, Moseley ME. Navigated diffusion imaging of normal and ischemic human brain. Magn Reson Med 1995;33:720–728.

18. Warach S, Gaa J, Siewert B, Wielopolski P, Edelman RR. Acute human stroke studied by whole brain echo planar diffusion-weighted magnetic resonance imaging. Ann Neurol 1995;37:231–241.

19. Makris N, Worth A, Sorensen A, Papadimitriou G, Wu O, Reese T, Wedeen V, Davis T, Stakes J, Caviness V, Kaplan E, Rosen B, Pandya D, Kennedy D. Morphometry of in vivo human white matter association pathways with diffusion-weighted magnetic resonance imaging. Ann Neurol 1997;42:951–962.

20. Werring DJ, Clark CA, Barker GJ, Miller DH, Parker GJ, Brammer MJ, Bullmore ET, Giampietro VP, Thompson AJ. The structural and functional mechanisms of motor recovery: complementary use of diffusion tensor and functional magnetic resonance imaging in a traumatic injury of the internal capsule. J Neurol Neurosurg Psychiatry 1998;65:863–869.

21. Neil JJ, Shiran SI, McKinstry RC, Schefft GL, Snyder AZ, Almli CR, Akbudak E, Aronovitz JA, Miller JP, Lee BC, Conturo TE. Normal brain in human newborns: apparent diffusion coefficient and diffusion anisotropy measured by using diffusion tensor MR imaging. Radiology 1998;209:57–66.

22. Huppi PS, Maier SE, Peled S, Zientara GP, Barnes PD, Jolesz FA, Volpe JJ. Microstructural development of human newborn cerebral white matter assessed in vivo by diffusion tensor magnetic resonance imaging. Pediatr Res 1998;44:584–590.

23. Pierpaoli C, Basser PJ. Toward a quantitative assessment of diffusion anisotropy. Magn Reson Med 1996;36:893–906.

24. Conturo TE, McKinstry RC, Akbudak E, Robinson BH. Encoding of anisotropic diffusion with tetrahedral gradients: a general mathematical diffusion formalism and experimental results. Magn Reson Med 1996;35:399–412.

25. Westin CF, Peled S, Gudbjartsson H, Kikinis R, Jolesz FA. Geometrical diffusion measures for MRI from tensor basis analysis. In: Proceedings of the 5th Annual Meeting of ISMRM, Vancouver, 1997. p 1742.

26. Ulug AM, van Zijl PC. Orientation-independent diffusion imaging without tensor diagonalization: anisotropy definitions based on phys-ical attributes of the diffusion ellipsoid. J Magn Reson Imaging 1999; 9:804–813.

27. Basser PJ, Mattiello J, LeBihan D. MR diffusion tensor spectroscopy and imaging. Biophys J 1994;66:259–267.

28. Coxeter HSM. Introduction to geometry. New York: John Wiley & Sons, Inc.; 1969.

29. Kindlmann G, Weinstein D. Hue-balls and lit-tensors for direct volume rendering of diffusion tensor fields. In: Proceedings of the IEEE Visualization 1999; abstract P7-1.

30. Bastin ME, Armitage PA, Marshall I. A theoretical study of the effect of experimental noise on the measurement of anisotropy in diffusion imaging. Magn Reson Imaging 1998;16:773–785.

31. Basser PJ, Pierpaoli C. A simplified method to measure the diffusion tensor from seven MR images. Magn Reson Med 1998;39:928–934.

32. Alexander A, Tsuruda J, Parker D. Elimination of eddy current artifacts in diffusion-weighted echo-planar images: the use of bipolar gradients. Magn Reson Med 1997;38:1016–1021.

33. Haselgrove J, Moore J. Correction for distortion of echo-planar images used to calculate the apparent diffusion coefficient. Magn Reson Med 1996;36:960–964.

34. Shimony JS, McKinstry RC, Akbudak E, Aronovitz JA, Snyder AZ, Lori NF, Cull TS, Conturo TE. Quantitative diffusion-tensor anisotropy brain MR imaging: normative human data and anatomic analysis. Radiology 1999;212:770–784.

35. Falconer JC, Narayana PA. Cerebral spinal fluid-suppressed high-resolution diffusion imaging of human brain. Magn Reson Med 1997;37: 119–123.

36. Hirsch JG, Bock M, Essig M, Schad LR. Comparison of diffusion anisotropy measurements in combination with the FLAIR-technique. Magn Reson Imaging 1999;17:705–716.

37. Zacharopoulos NG, Narayana PA. Selective measurement of white matter and gray matter diffusion trace values in normal human brain. Med Phys 1998;25:2237–2241.

38. Bahn MM. Comparison of scalar measures used in magnetic resonance diffusion tensor imaging. J Magn Reson 1999;139:1–7.